Chapter 2

The LEP Accelerator and the LEP Beam Energy Measurement

2.1 Introduction

In this chapter the LEP accelerator will be described. Emphasis will be placed on the LEP beam energy calibration, in particular on the LEP Spectrometer, given its importance as a source of uncertainty in the measurement of the W mass.

2.2 The Accelerator

The Large Electron–Positron collider (LEP) is an e^+e^- collider located on the French-Swiss border at the European Laboratory for Particle Physics (known by its French acronym CERN) on the outskirts of Geneva, as shown in Figure 2.1. Its main ring has a circumference of 26.7 km making it the world's largest collider. Built on a stable layer of rock at an average depth of 100m below the surface, it comprises a series of alternated straight sections and arcs. The arcs contain some 3300 dipole magnets to bend the beams, quadrupole and sextupole magnets for focusing, and dedicated dipoles for correcting the horizontal and vertical position of the beams. The eight straight sections contain the Interaction Points (IPs) where the paths of the e^+, e^- beams traveling in opposite directions meet. In the four straight sections, where the multi-purpose detectors ALEPH, DELPHI, L3 and OPAL (ADLO) are situated, the beams are made to collide at the IPs. Otherwise they are steered away from each other at crossover to avoid unnecessary loss of beam current. In addition to the four detectors, the straight segments contain the RF cavities which restore the energy lost by the beams to synchrotron radiation. The reason for placing the detectors in the straight sections is to protect them from this synchrotron radiation. Before discussing the beam acceleration process in the main ring any further, the beam pre-acceleration and injection chain will be outlined.

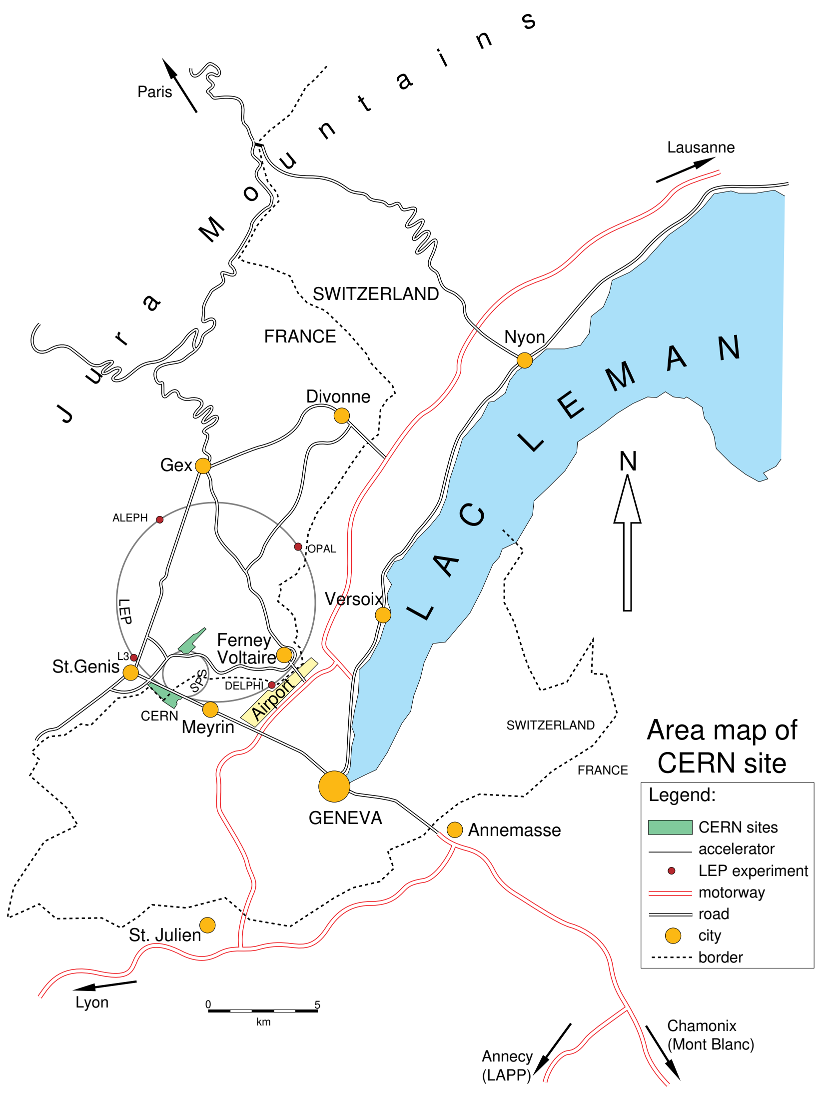

Figure 2.1: The location of the CERN laboratory and the LEP accelerator.

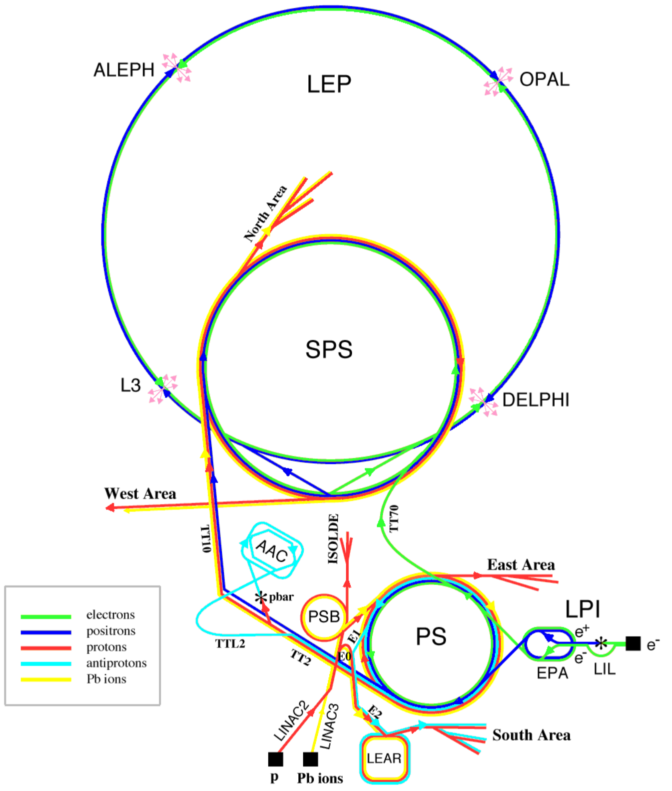

EPA - Electron Positron Accumulator
LEP - Large Electron Positron collider
LIL - LEP Injector Linac
LPI - LEP Pre-Injector
PS - Proton Synchrotron
SPS - Super Proton Synchrotron

Figure 2.2: A diagram of LEP with the pre–accelerators and injection system. The acronyms used for the accelerators which make up the LEP system are given. The other particle accelerators at CERN are also shown. This diagram is not to scale.

2.3 The e^+e^- Injection Chain

A schematic of the acceleration and injection chain into the LEP ring is shown in Figure 2.2. The process involves many accelerators which were already in existence before LEP. The injection and acceleration process can be summarised as follows:

- Electrons from a high intensity source are accelerated to an energy of 200 MeV by the LEP Injection LINAC (LIL). This electron beam is made to hit a tungsten target to produce positrons.
- A lower intensity source produces electrons. Both electrons and positrons are accelerated by the LIL to an energy of 600 MeV.

Year	Copper Cavities	Superconducting Cavities	E_{BEAM} (GeV)	$\int \mathcal{L}dt$ (pb^{-1})
1995	120	56	70.1	6.9
1996	120	170	86.2	23.4
1997	86	240	92.0	71.0
1998	48	272	94.4	181.9
1999	48	288	95.8	29.1
			97.8	85.4
			99.8	91.1
			100.8	44.0

Table 2.1: The RF cavity configuration of LEP (at the end of each year), the maximum E_{BEAM} and the integrated luminosity delivered to DELPHI in 1995 to 1999

- Both beams are stored in the Electron Positron Accumulator (EPA) until their currents are large enough.
- The beams are injected into the Proton Synchrotron (PS) and accelerated until they reach an energy of 3.5 GeV.
- The beams are moved into the Super Proton Synchrotron (SPS)and accelerated to an energy of 20 to 22 GeV. They are then injected into the main LEP accelerator.
- In the main accelerator the beams are ramped up in steps to nominal physics energy. During ramping the beams are deflected by electrostatic separators at the IPs in order to keep them from colliding.

After the acceleration cycle the beams are kept colliding at physics energy until they are lost or until the beam current is too low, in which case they are dumped and the cycle re-started.

2.4 The RF System

The increases in RF power in LEP have been have been driven by the objective to run at higher and higher centre of mass energies. Whereas during LEP1 operation 120 copper RF cavities with an accelerating field of 1.5 MVm^{-1} were sufficient, running at LEP2 energies has required a radical upgrade of the RF system, with the replacement of most Cu cavities by superconducting Nb-Cu and Nb ones with a maximum accelerating field of 7 MVm^{-1}, as detailed in Table 2.1. The main reason for such a significant increase in RF power is that the energy loss due to synchrotron radiation of a beam of energy E_{BEAM} following a curve of radius ρ is proportional to E^4_{BEAM}/ρ. So while the energy loss per turn in LEP1 was typically 0.13 GeV for an E_{BEAM} of 45 GeV, for an E_{BEAM} of 100 GeV it is $\sim$ 3 GeV. The increase in available accelerating potential and further improvements to the reliability of the accelerator allowed for stable running with beam energies of $\sim$ 94.3 GeV and up to $\sim$ 101 GeV in 1998 and 1999 respectively[1]. Furthermore, the integrated luminosities for these two running periods exceeded the anticipated values [28, 29].

2.5 Luminosity

The instantaneous luminosity, $\mathcal{L}$, of an accelerator is given, to a good approximation, by

$$\mathcal{L} = \frac{n_b I_b^2}{4\pi e^2 f \sigma_x \sigma_y}, \tag{2.1}$$

where n_b is the number of bunches per beam, I_b is the bunch current, e is the charge of the electron, f is the LEP revolution frequency (10.8 kHz) and σ_x and σ_y are the horizontal and vertical beam widths respectively. In 1998 and 1999 LEP ran in 4-bunch mode achieving instantaneous luminosities of $\sim 10^{32}$ $\mathrm{cm}^{-2}\mathrm{s}^{-1}$, close to a factor of 5 higher than at LEP1. This increase was driven by a reduction of the beam widths σ_x and σ_y and by an increase in the bunch current I_b. Typical values for these parameters during the 1998 and 1999 running periods were σ_x $\sim$170μm ($\sim$0.7 of LEP1 value), σ_x $\sim$3.5μm ($\sim$0.25 of LEP1 value), and I_b $\sim$800μm ($\sim$1.3 of LEP1 value). In order to control the beam width, a series of superconducting quadrupole magnets are used to tightly focus the beam. A further enhancement can be achieved by using the electrostatic beam deflectors. The improvements in focusing and bunch current are detailed in [30, 31, 28]. The integrated luminosities, $\int \mathcal{L} dt$, delivered to DELPHI between 1995 and 1999 are shown in Table 2.1.

[1] In 1999 LEP ran with stable luminosity conditions at four nominal energy points with beam energies of 96, 98, 100 and 101 GeV.

2.6 Energy Calibration

The LEP beam energy contributes directly to the overall uncertainty of the measurement of $\mathrm{M_W}$ due to the use of constrained kinematic fits to extract event by event observables, like the fitted invariant mass m_w. The contribution goes, to a good approximation, as:

$$\frac{\Delta \mathrm{M_W}}{\mathrm{M_W}} \approx \frac{\Delta E_{\mathrm{BEAM}}}{E_{\mathrm{BEAM}}}. \tag{2.2}$$

With an integrated luminosity of $\sim 700\mathrm{pb}^{-1}$ collected per experiment by the end of the LEP2 programme, the statistical uncertainty on $\mathrm{M_W}$ will be close to 21 MeV. To meet the target total uncertainty on $\mathrm{M_W}$ of $\sim$ 35 MeV the uncertainty on the beam energy must be controlled to $\Delta E_{\mathrm{BEAM}}/E_{\mathrm{BEAM}} \approx 10^{-4}$. During LEP1 the precision on E_{BEAM} was controlled to 2×10^{-5} [32]. Such precision is currently not possible at LEP2 for reasons that will be explained below, and new methods have been developed and implemented in the quest to reach the required sensitivity. First the salient points of the current energy calibration method will be outlined, and then some improvements will be discussed.

2.6.1 Resonant Depolarisation

At LEP1 the beam energy was measured to great precision using resonant depolarisation (RDP) [32]. This technique exploits the fact that the $e^{\pm}$ beams develop appreciable transverse polarisation due to the emission of synchrotron radiation as their trajectory changes in the magnetic field of the dipoles. The spin vectors precess about the field lines of the dipoles with a frequency given by:

$$f_p = f_{\mathrm{LEP}} \frac{(g_e - 2)}{2} \frac{E_{\mathrm{BEAM}}}{m_e c^2}, \tag{2.3}$$

where $(g_e - 2)/2$ is the anomalous magnetic moment of the electron, m_e is the mass of the electron and c is the speed of light, all known to great accuracy, and f_{LEP} is the LEP revolution frequency. The number of spin precessions per revolution around LEP is the *spin tune*, given by:

$$\nu_p = \frac{f_{\mathrm{LEP}}}{f_p}. \tag{2.4}$$

It is ν_p that is probed experimentally through RDP. By applying a transverse sinusoidal magnetic field of frequency f_{RDP} to the beam the polarisation can be destroyed. As the beam only passes through the depolarising region once per revolution of LEP, the condition for this depolarisation is that f_{RDP} divided by f_{LEP} match the non-integer part of ν_p. The integral part must be calculated by the use of flux loop and nuclear magnetic resonance (NMR) measurements, which are described in the following section. The measurement of the beam polarisation is performed with the LEP polarimeter apparatus [33]. It is a device which brings a circularly polarised laser beam into interaction with the electron and positron beams. The rate of Compton backscattered photons is monitored by a calorimeter as a function of the vertical direction for right and left handed laser beams. The asymmetry in the distributions is sensitive to the degree of transverse polarisation in the electron beam.

Using RDP, E_{BEAM} was determined to 1 part in 10^5 at LEP1 , greatly increasing the sensitivity of the high precision measurements carried out at the Z^0 resonance. Unfortunately the RDP technique is not applicable at LEP2 energies due to incoherent depolarisation effects caused by machine imperfections and which increase rapidly with beam energy. The result is that the $\sim 5\%$ level of polarisation necessary for a reliable energy measurement has not been observed at beam energies beyond 61 GeV. Therefore the current strategy relies on NMR magnetic measurements and extrapolation.

2.6.2 The Extrapolation Method

Since E_{BEAM} is proportional to the magnetic field B integrated along the beam's trajectory l around LEP:

$$E_{\text{BEAM}} = \frac{e}{2\pi c} \oint_{\text{LEP}} B \cdot dl. \tag{2.5}$$

the beam energy can in principle be measured from estimates of $\oint_{\text{LEP}} B \cdot dl$. The integrated bending field is estimated from continuous measurements of the local magnetic fields by 16 NMR probes placed in some of the 3300 LEP main dipole magnets. The probes can measure the local field with a relative precision of $\sim 10^{-6}$

and can provide reliable measurements down to 40 GeV, although this minimum locking energy increases with radiation damage. For this reason probes have to be replaced through the year, but great care is taken to position them with accuracy in order not to be affected by variations in the local field in the vicinity of the probe. Even though the probes only sample a minute fraction of the total bending field, its relation to E_{BEAM} can be calibrated with great precision at low energies against measurements from RDP. Assuming a linear dependence of the local B field on the mean E_{BEAM}, each probe i is calibrated using:

$$E^{RDP}_{NMR\ i} = a_i B_{NMR\ i} + b_i, \tag{2.6}$$

during dedicated multi-point RDP fills, where the same beam is ramped to a set of nominal energies ranging from 41 to 61 GeV and RDP performed where possible. A fit to all available RDP energy points is made, regardless of the fill the data were taken in. In practice other time-dependent effects that affect the relation between the dipole field and the beam energy, such as the C corrections shown in Equation 2.7, are taken into account in the calibration 2.6, thereby normalising the calibration to a given set of conditions.

The beam energy model

Since the NMR probes only give a measurement of the contribution to the total bending field due to the main dipoles, all other effects that may contribute to $\oint B_{\mathrm{LEP}} \cdot dl$, as well as time-dependent effects which may alter the relation between $E_{\mathrm{BEAM}}(RDP)$ and each B_{NMR}, have to be taken into account separately and put into what is known as the *beam energy model* [32, 34], which gives the average beam energy around the accelerator as a function of time, $E_{\mathrm{BEAM}}(t)$. For LEP2, the model can be expressed as[2]:

$$\begin{aligned} E_{\mathrm{BEAM}}(t) &= (E_{\mathrm{initial}} + \Delta E_{\mathrm{dipole}}(t)) \\ &\cdot(1 + C_{\mathrm{tide}}(t)) \cdot (1 + C_{\mathrm{orbit}}(fill)) \\ &\cdot(1 + C_{\mathrm{h.corr.}}(t)) \cdot (1 + C_{\mathrm{QFQD}}(t)) \end{aligned} \tag{2.7}$$

[2] The beam energy model at LEP1 differed from Equation 2.7 in some aspects. The normalisation was treated differently because magnetic extrapolation was not necessary at the Z^0. Furthermore, the correction $\Delta E_{\mathrm{dipole}}(t)$ was implemented differently because of more sparse magnetic sampling.

where E_{initial} is the energy averaged from the $E^{RDP}_{NMR\ i}$, extracted from Equation 2.6, of each probe at the time when the dipole magnets have reached operating conditions. Here, equal weight is given to each probe in the average since each magnet behaves differently during LEP ramping. $\Delta E_{\text{dipole}}(t)$ gives the shift in energy due to changes in the bending field of the dipoles during a fill. These changes, due to temperature variations[3] and excitation of parasitic currents in the beam pipe, are considered to be traced by the calibrated NMRs and so are also calculated from a mean of the $E^{RDP}_{NMR\ i}$, this time with equal weight given to each of the octants, since these effects vary octant by octant [32]. The remaining terms in Equation 2.7 correct for other time-dependent effects:

$C_{\text{tide}}(t)$: The earth tides distort the shape of the LEP ring, effectively moving the quadrupole magnets with respect to the beam orbit. Beams passing off-centre through the quadrupoles sample more of the dipole component of the quadrupole field.

C_{orbit}: This term corrects for longer time scale horizontal drifts of the beam orbit and is evaluated for each fill.

$C_{\text{RF}}(t)$: This accounts for the changes in RF frequency during a fill which are made to optimise luminosity and to respond to RF trips.

$C_{\text{h.corr.}}(t)$: This term takes into account the extra bending field provided by the horizontal orbit corrector magnets which are used to steer the beam.

$C_{\text{QFQD}}(t)$: This accounts for the stray fields caused by the difference in the excitation currents used for focusing and defocusing quadrupole magnets in LEP.

All the above corrections are explained in detail in [32, 35, 36]. They apply to the measurement of the mean beam energy around the LEP. The evaluation of E_{BEAM} at any given point in the accelerator takes into account factors that give deviations from the mean beam energy as a function of the position along the circumference of LEP.

[3] The difference in the temperature coefficients in the core of the magnet and in the fringe field mean that there is a real change in $\Delta E_{\text{dipole}}(t)$ which is not traceable by the NMR probes. To give an idea of the magnitude of the effect, the LEP spectrometer magnet was found to have an effective temperature coefficient of $\sim 10^{-5} K^{-1}$ (see section 2.7.5)

The main factor behind these asymmetries is the uneven distribution of RF power around LEP. This is of particular importance to the spectrometer energy calibration, since it measures the centre of mass energy locally. The RF model [32, 34] provides the energy corrections and associated errors necessary to evaluate the beam energy of the electron and positron beams at each of the IPs. Conversely, it can be used to infer the average beam energy around LEP from a local measurement, like that provided by the spectrometer.

Testing the NMR calibration with the flux loop

In the RDP energy range, the relation between NMR values and E_{BEAM} is linear to a good approximation. The assumption is made that this linearity holds up to physics energies and the NMR values then play the leading role in the determination of E_{BEAM} values. This assumption can be checked against an independent measurement of the field integral. Each of the LEP main dipoles is fitted with a flux loop. The flux loops (FLs) can provide a measurement of $\sim$ 98% of the field of each of the 3300 main bending dipoles and $\sim$ 96% of the total bending field of the accelerator. They exclude the fringe fields of the main dipoles and the bending field from the weak dipoles placed at the ends of the arcs, and any bending field contribution provided by quadrupoles, sextupoles and dipole orbit correcting magnets.

The change in flux through the loops is measured during dedicated cycles where the magnets are ramped up through a series of nominal energy points including the RDP region and going up to physics energies. At each energy the cycle is paused for the NMR probes to lock and average values of their readings calculated. The linear extrapolation assumption can then be checked by fitting the NMR values in the RDP region to the 96.5% of the total bending field provided by the flux loops according to Equation 2.5, in a manner similar to 2.6:

$$E_{NMR\ i}(FL) = c_i B_{NMR\ i} + d_i. \tag{2.8}$$

Here, the flux loop reading has been represented as an energy by way of analogy with Equation 2.6. Then the prediction of the total field from the NMRs at physics energies can be compared to that given by the flux loop. The discrepancy between

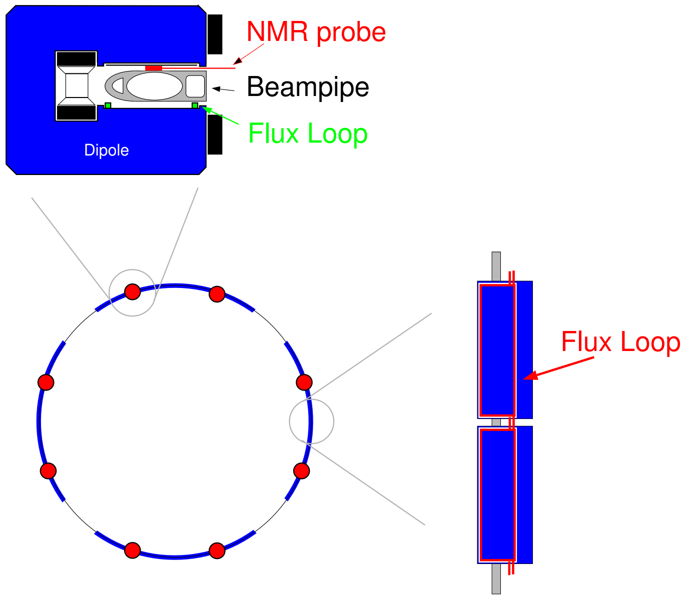

Figure 2.3: A schematic of the positioning of flux loops and NMR probes on a LEP main dipole.

the NMR and flux loop measurements, which can be seen for the 1999 data in Figure 2.4, lead to the dominant error on $E_{\rm BEAM}$ of 15 MeV in 1998 and 1999[4].

Since the uncertainty in the extrapolation, currently given by the flux loop experiments, is the dominant contribution to the total error on $E_{\rm BEAM}$, alternative methods have been developed to perform independent measurements of $E_{\rm BEAM}$ at physics energies with a view towards improving the confidence in the extrapolation and thereby ensuring a total relative error to the of 10^{-4}. Two such methods, the synchrotron tune Q_s and the LEP spectrometer, shall be described in the following sections, with emphasis placed on the latter. A third method, based on the reconstruction of the effective centre of mass energy from the three-body kinematics of the radiative two fermion $e^+e^- \rightarrow f\overline{f}\gamma$ process, can be performed by the individual experiments. For details of this method the reader is referred to [37, 38] and references therein.

[4] This is the dominant contribution to an error of 20 and 21 MeV in 1998 and 1999 respectively.

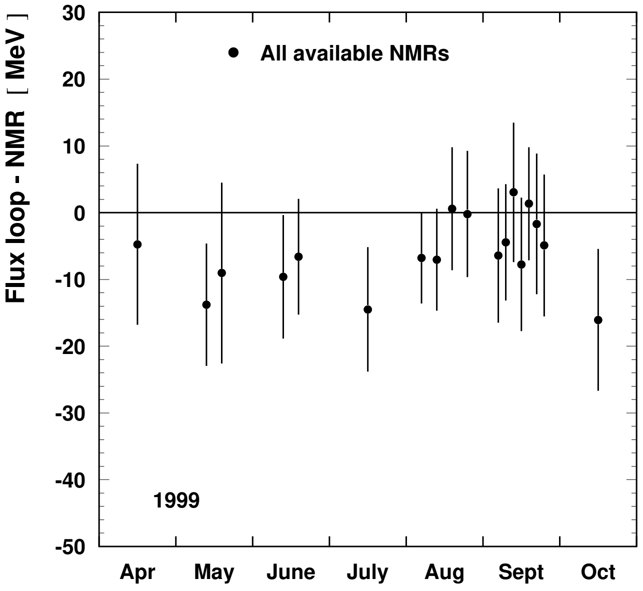

Figure 2.4: Residual difference between Flux Loop and NMR predictions of $\int B \cdot dl$ expressed as E_{BEAM}. Both methods are cross-calibrated in the RDP range and the results in the physics energy range compared. The plot shows the data taken in 1999.

2.7 The LEP Spectrometer

2.7.1 Introduction

The purpose of the LEP Spectrometer is to provide a direct measurement of E_{BEAM} at the M_W scale by measuring the local beam energy through:

$$E_{\text{Spect}} = \frac{1}{\theta} \int B \cdot dl_{\text{Spect}}, \tag{2.9}$$

where E_{Spect} now refers to the *local* beam energy as the beam traverses a bending field $\int B \cdot dl_{\text{Spect}}$ and is deflected by an angle θ. The basic principle behind the spectrometer concept is shown in Figure 2.5. The spectrometer is integrated into the LEP magnet lattice. Two of the 3300 concrete LEP dipole magnets were replaced with a high precision steel dipole with twice the bending field, such that the beam deflection angle θ is fixed within the allowable variations of the beam orbit, while the integrated bending field $\int B \cdot dl_{\text{Spect}}$ varies with the rest of the LEP dipoles as E_{BEAM} changes. Compared to the concrete core magnets, the steel one produces a field more uniform with respect to time and position, has a lower temperature

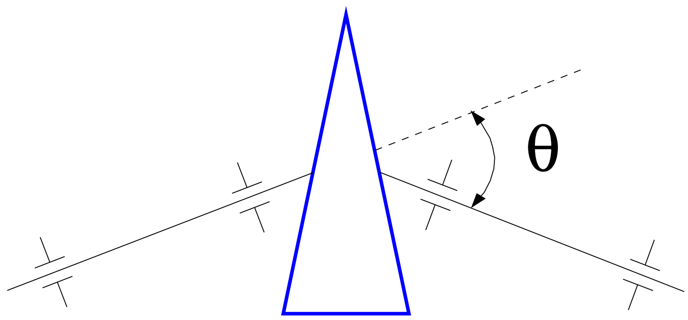

Figure 2.5: The spectrometer measures the beam deflection θ and the integrated bending field $\int B \cdot dl_{\mathrm{Spect}}$ of a dipole magnet in order to provide a measurement of the local beam energy.

coefficient, and does not have the long term drifts in field due to ageing which have been observed in the standard LEP dipoles. The general layout of the spectrometer is outlined below. There follows a section on the strategy used to measure E_{BEAM} with the spectrometer. The details of the measurements of the beam deflection and integrated bending field are given in Sections 2.7.4 and 2.7.5.

2.7.2 Layout

The LEP Spectrometer can be divided into beam bending and monitoring apparatus. A schematic of the layout of the is given in Figure 2.6. The bending apparatus consists of a 5.75m long C-shaped laminated steel dipole magnet. It is equipped with a water cooling system in order to maintain the temperature constant to within 1^oC, probes monitoring the temperature in different sections of the magnet, and four NMR probes placed in its core to monitor the changes in local fields in the magnet. Two types of NMR probes are used. These are referred to as "Range Type 1" and "Range Type 2" and they cover different ranges of magnetic field. There are two of each type mounted in the core of the magnet. Type 1 probes saturate at magnetic fields corresponding to nominal energies beyond $\sim$ 60 GeV, while type 2 probes are operational from $\sim$ 40 GeV upwards. However, with radiation damage, their locking threshold rises so the two types are necessary to ensure that readings are available for the full energy range under normal LEP running conditions. The integrated bending field of the magnet, $\int B \cdot dl_{\mathrm{Spect}}$, can be inferred from the local fields measured by the four NMR probes and other environmental variables, like the temperature of different parts of the magnet. The author developed the algorithms and software used for this purpose. The end fields and stray fields from the steel dipole and other magnets in the lattice are suppressed by a mu-metal shield which surrounds the beam pipe at either end of the magnet.

The beam monitoring apparatus consists of two arms of beam position monitors (BPMs). Each arm has three BPMs and is equipped with stretched wire position monitors, synchrotron radiation copper absorber blocks, temperature probes and a water cooling system. The BPMs are ~4m apart, giving a lever arm of ~10m. There is one arm at each end of the dipole magnet. The triplets of BPMs on each arm measure the beam trajectory at either side of the magnet and hence the beam deflection angle θ.

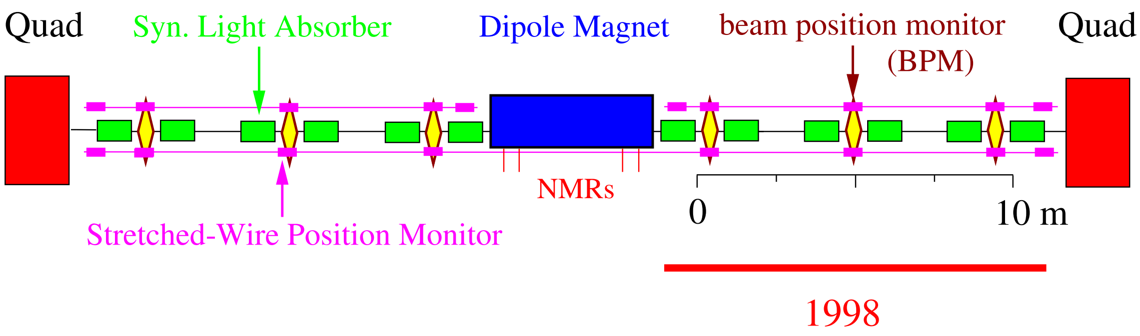

Figure 2.6: The layout of the LEP spectrometer showing the steel dipole magnet, the beam position monitors, the synchrotron radiation absorber blocks and the stretched wire position monitors. In 1998, a single-arm prototype was in place.

2.7.3 E_{BEAM} Measurement Strategy

The required accuracy on E_{BEAM} of 10^{-4} translates into a maximum relative error on the bend angle θ of 10^{-4}. Whereas an absolute precision on θ of this magnitude is unattainable, a high precision relative measurement is possible by calibrating the bend angle against RDP at low energies. The changes in deflection angle and $\int B \cdot dl_{\text{Spect}}$ can be then used to trace the beam energy as LEP is ramped up to physics energies. The strategy adopted can be visualised in Figure 2.7. It is summarised as follows:

- The beam is steered to the nominal trajectory and the BPM gain calibration is performed (see section 2.7.4).

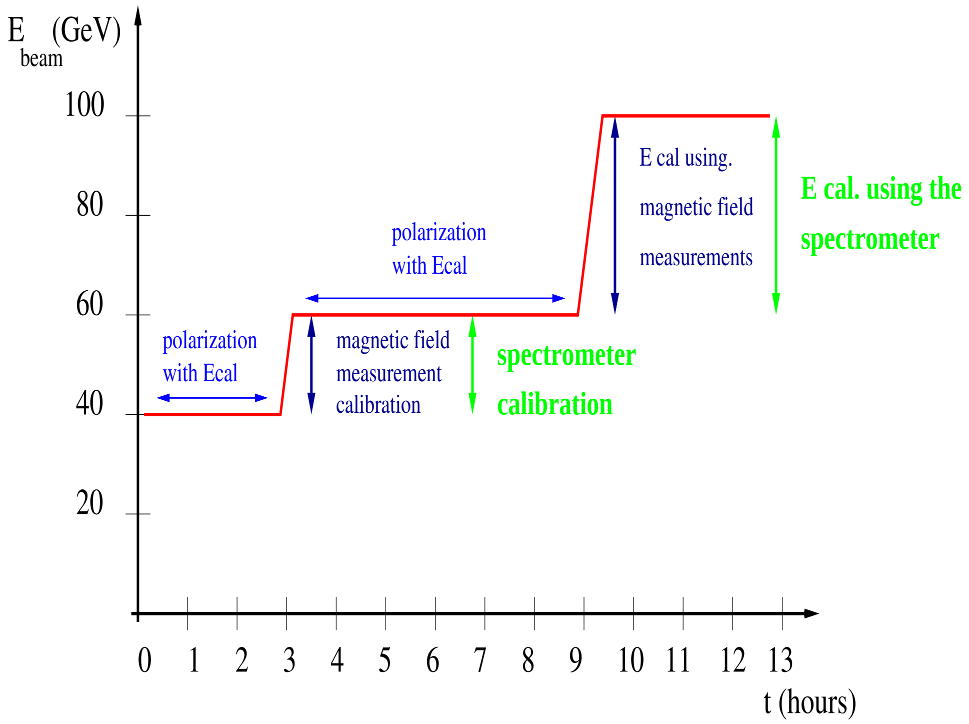

Figure 2.7: A schematic of the $E_{\rm BEAM}$ calculation using the spectrometer. The spectrometer is first calibrated against RDP measurements. The beam is then ramped to physics energies and the beam energy calculated using the spectrometer. Magnetic measurements with the NMR extrapolation method are performed in parallel and the two results compared.

- The Spectrometer is calibrated against RDP at low energies, $E_{\rm RDP}$. Here, the local beam energy measured at the location of the spectrometer, octant 3 or P3, is translated to $E_{\rm BEAM}$ using the the RF model. This energy is calibrated against RDP, effectively constraining the beam deflection angle through Equation 2.9. This does away with the need to measure absolute deflection angles θ.

- The beam is ramped up to physics energies, $E_{\rm Phys}$ and steered to the nominal trajectory.

- The BPM gain calibration is performed again.

- The beam energy is adjusted by varying the RF frequency such that $\theta_{\rm RDP}$ is close to $\theta_{\rm Phys}$.

- A relative beam energy measurement is performed from the *ratio* of the two bending angles θ_{RDP} and θ_{Phys}, and that of the bending fields of the dipole at both energies:
$$\frac{E_{Phys}}{E_{RDP}} = \frac{\int B \cdot dl_{\text{Spect}}|_{E_{Phys}}}{\int B \cdot dl_{\text{Spect}}|_{E_{RDP}}} \frac{\theta_{RDP}}{\theta_{Phys}}. \tag{2.10}$$
The dependence on the calibration of the absolute BPM gains is minimised in the limit that $\theta_{\text{RDP}} = \theta_{\text{Phys}}$, since large sources of error affecting the change in beam deflection, like the absolute gain and the change in BPM button signals, are avoided.

- The predicted mean beam energies for the calibrated spectrometer at low energy are then compared to those obtained from RDP to check for linearity.

- The mean beam energies predicted by the spectrometer, E_{Spect} at higher energies are compared to those obtained from the NMR model. Thus, provided the spectrometer behaves well in the RDP region, it serves as a test to confirm or reject the assumption of the linear relation between the NMRs and the LEP total bending field.

2.7.4 Measurement of Beam Deflection θ

The beam deflection is measured using three BPMs on either side of the dipole magnet, in areas of zero field. They are numbered 6, 5, 4, 1, 2, 3 in increasing z direction, that is, the direction of motion of the e^- beams. Their positioning relative to the dipole can be seen in Figure 2.6. The lever arm of each triplet is close to 10m. Given the target relative accuracy on E_{BEAM} of 10^{-4} and the relative accuracy on $\int B \cdot dl_{\text{Spect}}$ of 3×10^{-5}, the required relative accuracy on the beam deflection angle θ is $\Delta\theta/\theta \sim 10^{-4}$. This translates to an accuracy of $\sim 1\mu$m in the measurement of the x position of the beam for each BPM. The BPMs must be stable at this level against mechanical and electronic drifts and fluctuations. The beam spectrometer energy calibration strategy used means that stability of this order is only required for a few hours while the spectrometer is calibrated against RDP (see section 2.7.3). However, with ~ 1 kWm^{-1} of power radiated as synchrotron light at physics energies, the whole spectrometer setup is in a very hostile environment. In order to keep thermal expansion of the BPM assemblies and the dipole magnet to a minimum, both are equipped with dedicated temperature sensors and water cooling stations. These allow temperature monitoring and control with higher accuracy than is possible with the standard equipment in the rest of LEP, giving the BPMs a thermal stability of $\pm 0.2^{o}C$. A stretched-wire positioning system measures any remaining thermal motion, which can be corrected for offline. The BPM buttons

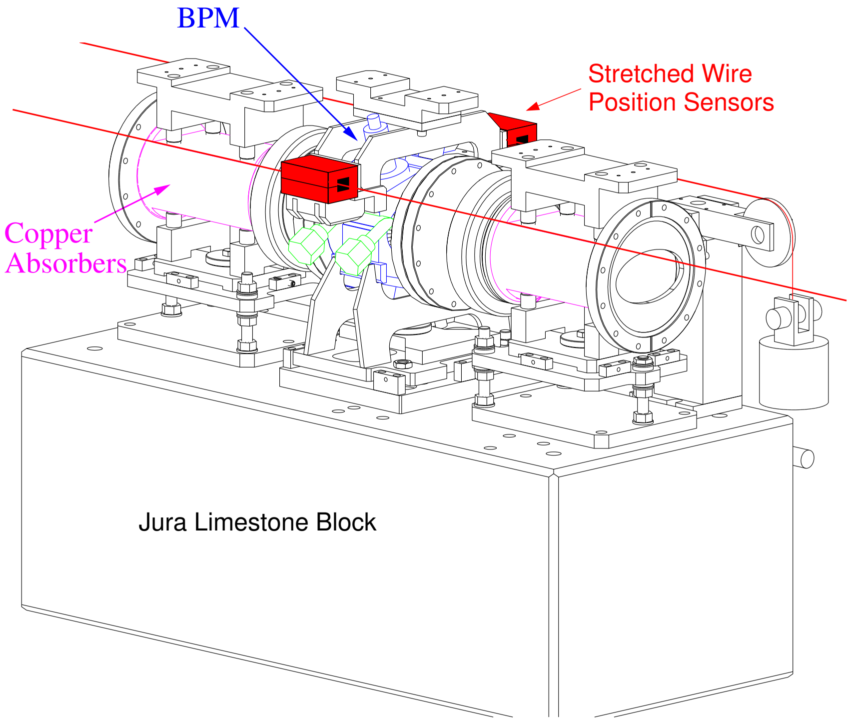

Figure 2.8: A BPM station showing the synchrotron light copper absorbers and the stretched-wire position sensors.

are protected from synchrotron light by copper absorbers (see Figure 2.8).

The bend angle θ is calculated from the sum of triplet angles on each arm of the spectrometer. Using small angle approximations, it can be expressed in terms of the x positions X_i measured by the BPMs on either side of the magnet:

$$\theta = \frac{(X_4 - X_6)}{2d_{BPM}} - \frac{(X_3 - X_1)}{2d_{BPM}}, \tag{2.11}$$

where X_6 (X_4) and X_3 (X_1) are the BPMs furthest (nearest) from the magnet on either side and d_{BPM} is the distance between two neighbouring BPM stations ($\approx$4m).

In order for the absolute error on the calibration of the BPM electronics cards not to have a large impact on the accuracy of the beam position measurements, and to reduce the effects of beam orbit drifts, a relative calibration method using controlled beam trajectory shifts is applied [39] to each arm separately. The purpose is to calibrate the gain of the exterior BPMs, 1 and 3 (4 and 6), to the central one, 2 (5), on either side. Taking one arm of the spectrometer for clarity (BPMs 1 to 3), the calibration procedure is as follows:

- Angular bumps are applied to the beam in the xz plane about BPM2:

$$X_3 = -X_1;\;\; X_2 = 0. \tag{2.12}$$

- Parallel beam bumps in the xz plane are applied:

$$X_1 = X_2 = X_3. \tag{2.13}$$

- Equations 2.12 and 2.13 represent two ideal lines that define an ideal plane:

$$X_2 = \frac{X_1 + X_3}{2}. \tag{2.14}$$

  The angles of the corresponding measured lines to the ideal plane give the relative gains of the BPMs. The gains of BPMs 1 and 3 are calibrated to that of BPM 2, shifting the measured lines to match the ideal plane.

- The resolution of the calibrated BPM triplets, and hence that of the relative θ accuracy, is calculated from the triplet residuals after the beam calibration has been applied:

$$T = X_2 - \frac{(X_1 + X_3)}{2}. \tag{2.15}$$

The x position of the beams as measured by each of the three BPMs on one arm of the spectrometer during the beam bumps described above, as well as the triplet residuals before and after calibration, are shown in Figure 2.9. The relative accuracy estimated from expression 2.15 is of 300nm over 1 hour, with individual BPM scatters of ~200nm. Hence the required relative accuracy of $\sim 1\mu$m has been surpassed. The reproducibility of the cross-calibration before and after an energy ramp

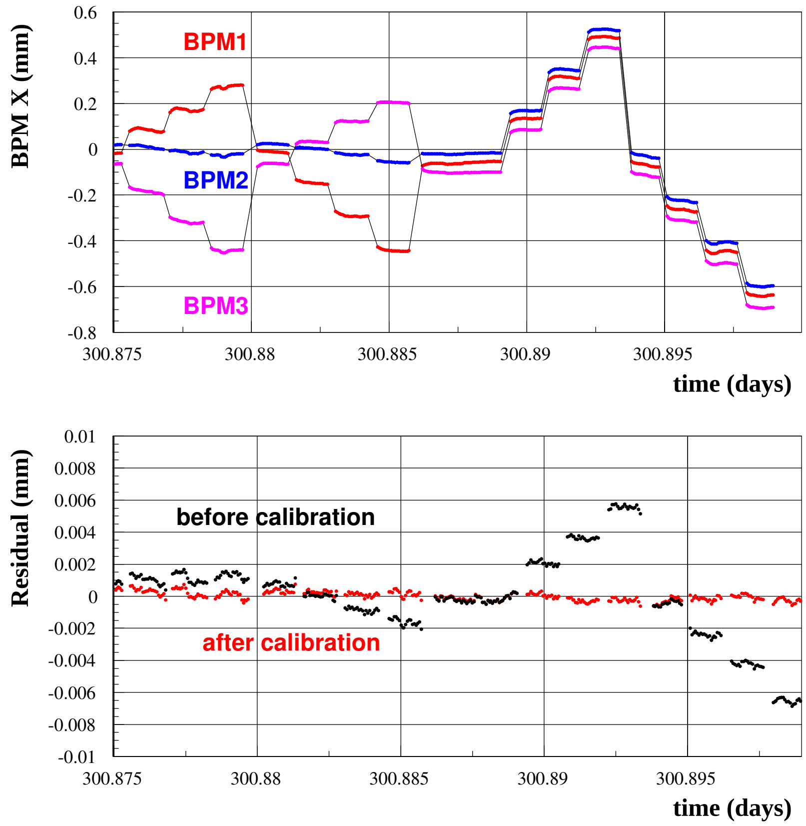

Figure 2.9: Beam based BPM gain cross-calibration. The beam is subjected to angular and parallel position changes which are followed by the three BPMs on one arm of the spectrometer (top). The triplet residuals before and after calibration are shown as a function of time (bottom).

is $\sim 10^{-3}$. The absolute gain can be calibrated using small frequency shifts δf_{RF} and comparing the fractional change in energy as determined by the spectrometer, given by

$$\frac{\delta E^{spect}_{\mathrm{BEAM}}}{E^{spect}_{\mathrm{BEAM}}} = \frac{\delta\theta}{\theta}, \tag{2.16}$$

to the fractional change in energy expected from the f_{RF} shift, given by

$$\frac{\delta E^{RF}_{\mathrm{BEAM}}}{E^{RF}_{\mathrm{BEAM}}} = -\alpha_c^{-1}\frac{\delta f_{RF}}{fRF}, \tag{2.17}$$

where α_c is the momentum compaction factor. The linear dependence between $\delta\theta/\theta$ and δf_{RF} can be seen in Figure 2.10. θ can then be calibrated to fit the expected slope, calculated in terms of f_{RF} and α_c.

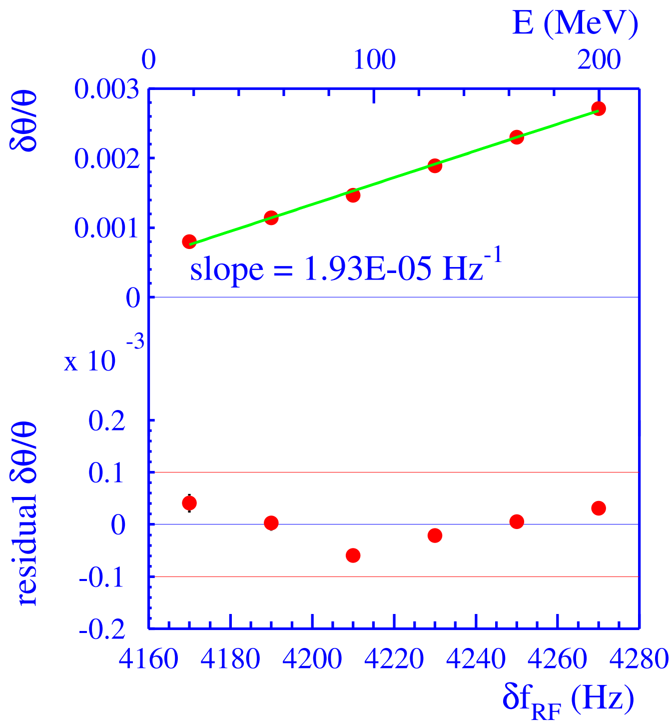

Figure 2.10: The observed relation between $\delta\theta/\theta$ and δf_{RF}. The slope depends on the absolute gain calibration of the BPMs. By fixing the slope to the expected value the absolute gain can be calibrated.

2.7.5 Measurement of $\int B \cdot dl_{\text{Spect}}$

The precision to which $\int B \cdot dl_{\text{Spect}}$ is known at different LEP regimes is crucial to the measurement of E_{BEAM} with the spectrometer. This section describes the procedures adopted to measure the integrated field of the dipole magnet under different conditions, how these measurements are related to those from the four NMR probes placed in the core of the magnet, and how the probes can be used to infer the integrated field of the magnet during LEP operations.

Mapping of the Spectrometer Dipole Magnet.

In order to have a precise knowledge integrated bending field of the LEP spectrometer magnet, $\int B \cdot dl_{\text{Spect}}$, an extensive mapping campaign was carried out between December 1998 and February 1999 in the old Interacting Storage Rings (ISR) tunnel at CERN. $\int B \cdot dl_{\text{Spect}}$ was measured in its totality under different temperatures and excitation currents. To achieve this, the magnet was scanned longitudinally by a measuring arm containing an NMR probe to measure local fields in its core with a relative precision of 10^{-6}, and with Hall probes to measure the fringe fields, which are too weak for NMR probes to lock, to a precision of $\sim 2.5 \times 10^{-4}$. The experimental setup for the mapping campaign is shown in Figure 2.11. Each standard

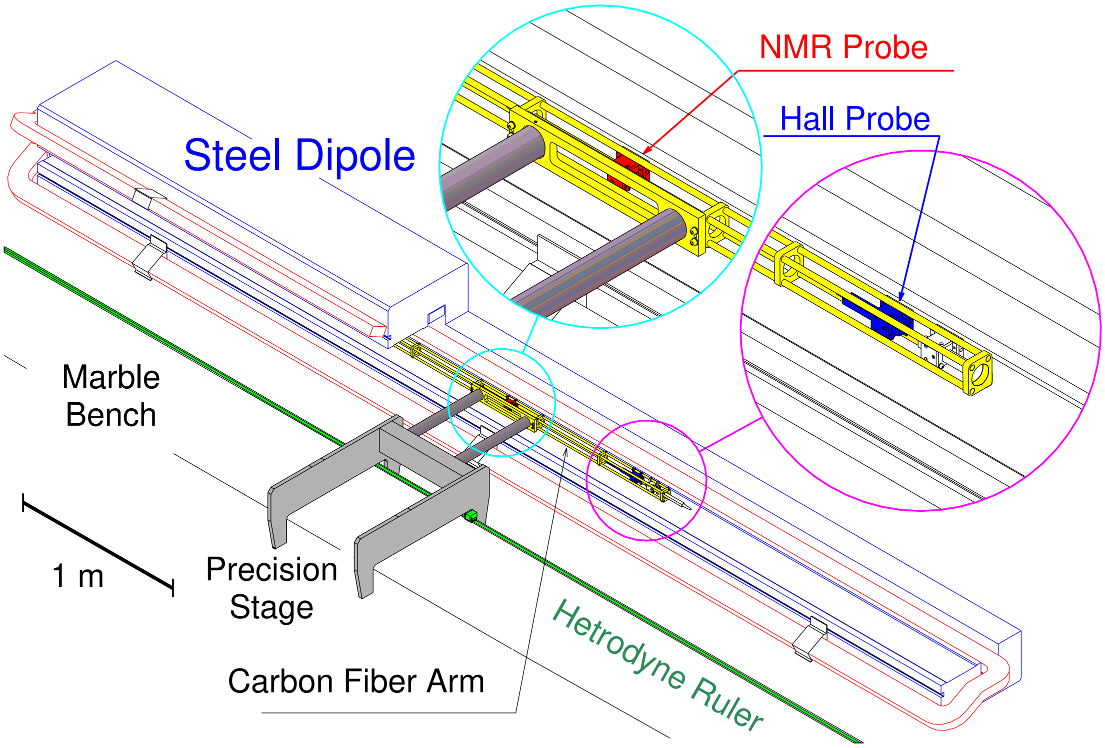

Figure 2.11: The Spectrometer mapping bench setup.

map contains a set of 552 readings taken at 1cm steps along the longitudinal axis of the magnet. The following quantities are logged: position, measured with a high precision ruler attached to the marble block (see Figure 2.11); NMR readings for the four stationary probes placed on the magnet; NMR and Hall probe readings for the moving arm; DC excitation current of the magnet; and temperatures for different parts of the dipole. During a standard map the temperature is kept constant to better than 1°C. The probe readings from the scanning arm can be used to calculate integrated fields along the longitudinal direction of the magnet using the trapezium method. The arm NMR readings are used directly to give the field at the core of the magnet. As the precision of the Hall probes is very poor compared

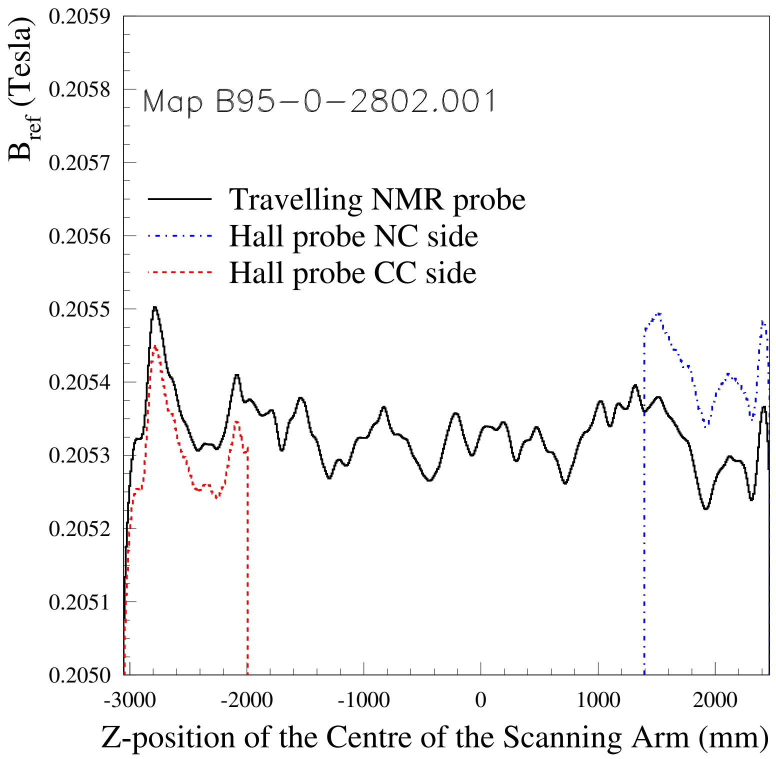

Figure 2.12: A magnet field map. The region of overlap between Hall and NMR probe readings points to discrepancies in the measured fields. These can be traced down to the inherent sensitivity of the Hall probes and a residual offset from mis-calibration. In practice, the offsets are corrected for and the scatter reduced by cross-calibration with the NMR. Since the fringe field only accounts for $\sim$ 10% of the total bending field this effect is not very significant.

to that of the NMR, it was necessary to calibrate them each map with the traveling NMR in a 150mm region of overlap at either end of the dipole, where both types of probe are operational. Figure 2.12 shows the discrepancy between Hall probe and NMR estimates of local fields in one map in the regions of overlap at either end of the magnet. As a first step, all Hall probe readings are scaled by a multiplicative factor $a_{Hall} = \overline{B^{Raw}_{HALL}}/\overline{B_{NMR}}$. A second effect discovered during the mapping campaign was that one of the Hall probes consistently gave field readings significantly different to zero in regions of the end-field where no field is expected, deep inside the mu-metal. Whether the effect was due to an instrumentation problem or to the existence of a real stray field was checked by performing measurements with an independent Hall probe in the region of interest. This experiment showed that the non-zero field was due to a problem with one of the Hall probes on the measuring arm, so a further correction b_{Hall} is applied to account for all offsets in the zero-field region. The offset is simply estimated from the mean value of the measured, local fields, $\overline{B_{Hall}^{mu-metal}}$, in a region ±65mm from the centre of the mu-metal, which is 845mm from the end of the magnet core. Both the a_{Hall} and b_{Hall} correction factors are calculated separately for each Hall probe and individually for each map. Each end-field reading from the Hall probes is then corrected for according to:

$$B_{Hall}^{Scale} = a_{Hall}(B_{Hall}^{raw} - b_{Hall}). \tag{2.18}$$

The relative RMS of the end-fields with and without these corrections, for maps taken at a nominal coil temperature of 34^oC[5], are shown in table 2.2. Although the calibration reduces the scatter, it is still large compared to that of the fields measured by the NMR probe, as can be seen in Table 2.3. However, the fact that the fringe field makes up only $\sim$ 10% of the total field means that the relative precision per map is $\sim 10^{-5}$, as was determined from the RMS scatter of maps taken under identical conditions. The end-field integrals are then re-evaluated from the scaled Hall probe readings using the trapezium method. The relative precision of these maps, determined by their reproducibility under "identical" conditions, ranges between 2×10^{-5} and 6×10^{-6} depending on the excitation current.

Stationary NMR probes

For each map, mean values of the B^i_{ref} fields measured by each one of the stationary NMR probes are also obtained after eliminating outliers and readings where probes were not locking[6]. While implementing this procedure, it was found that the scanning arm affects the local magnetic field seen by the stationary probes, as can be seen in Figure 2.13. The main effect is due to the passage of the traveling NMR probe over the reference ones. This effect disappears when the arm leaves

[5]The actual "nominal" temperature of a map refers to the mean temperature of the core of the dipole magnet. However, in the analysis that follows, only the temperature of the coil is used. For this reason, and to avoid confusion, the "nominal" temperatures given in what follows refer to coil temperatures only. The coil temperature is $\sim 4^oC$ higher than the core temperature.

[6]Non-locking NMR probes read out characteristic non-zero values which could be mistaken for genuine field values. Care has to be taken to identify these for each probe, and exclude them from the analysis.

Nominal Energy (GeV)	B^{raw}_{Hall}	$a_{Hall}B^{raw}_{Hall}$	$a_{Hall}(B^{raw}_{Hall} - b_{Hall})$
41	2.078×10^{-4}	1.806×10^{-4}	1.265×10^{-4}
44	2.497×10^{-4}	2.223×10^{-4}	2.264×10^{-4}
50	1.104×10^{-4}	8.866×10^{-5}	8.703×10^{-5}
55	1.325×10^{-4}	8.708×10^{-5}	6.537×10^{-5}
60	1.751×10^{-4}	1.450×10^{-4}	9.619×10^{-5}
70	1.085×10^{-4}	7.851×10^{-5}	4.958×10^{-5}
80	1.203×10^{-4}	9.302×10^{-5}	5.842×10^{-5}
90	8.317×10^{-5}	7.548×10^{-5}	4.356×10^{-5}
95	9.539×10^{-5}	7.446×10^{-5}	5.695×10^{-5}
100	2.642×10^{-4}	2.194×10^{-4}	6.762×10^{-5}
103	6.193×10^{-5}	5.425×10^{-5}	4.753×10^{-5}

Table 2.2: The relative RMS of the measured end-fields of maps for different nominal energies and for a nominal temperature of 34^oC. The first column corresponds to end-fields where no correction has been applied to the Hall probes. In the second column the probes have been scaled with a slope to the traveling NMR. Finally, the third column shows the spread when both a scaling and an offset correction have been applied. This two-parameter scaling is applied to the data on a map-by-map basis.

the vicinity of the reference probes and so future readings are not compromised. The average B field for each stationary probe is therefore calculated from readings where the arm is at a distance of $\geq$1400mm from the probe. Thus we have obtained an integrated bending field, a set of mean local field readings from the stationary probes with associated errors from the standard deviation, plus the temperature and excitation current information logged during each map of the magnet. This information will be used to derive a model which can infer an integrated bending field during LEP operations.

Calibrating the stationary NMR probes against the measured $\int B \cdot dl_{\mathbf{Spect}}$

Each stationary NMR probe is calibrated against the integrated bending field obtained from the traveling NMR and the corrected Hall probe readings. Using maps taken under different excitation currents and environmental conditions, a two parameter fit is used to determine the relation between total integrated fields and the mean value of each of the stationary probes, assuming a linear dependence:

$$\overline{B^i_{ref}} = m_i \int B \cdot dl + c_i, \tag{2.19}$$

where the index i corresponds to the four reference NMR probes. The fit is performed in the full nominal energy range, $E_{nom} = 41 \rightarrow 103$ GeV, despite the fact that the

Nominal Energy (GeV)	$RMS(B_{core})$	$RMS(B_{end})$	$RMS(B_{total})$
41	2.724×10^{-6}	1.265×10^{-4}	1.024×10^{-5}
44	9.453×10^{-5}	2.264×10^{-4}	1.032×10^{-4}
50	1.857×10^{-6}	8.703×10^{-5}	7.293×10^{-6}
55	1.329×10^{-6}	6.537×10^{-5}	5.343×10^{-6}
60	5.589×10^{-5}	9.619×10^{-5}	5.688×10^{-5}
70	3.998×10^{-6}	4.957×10^{-5}	6.249×10^{-6}
80	3.573×10^{-6}	5.842×10^{-5}	6.192×10^{-6}
90	5.104×10^{-6}	4.356×10^{-5}	6.955×10^{-6}
95	1.120×10^{-6}	5.695×10^{-5}	5.383×10^{-6}
100	1.954×10^{-5}	6.762×10^{-5}	1.399×10^{-5}
103	8.246×10^{-7}	4.753×10^{-5}	4.151×10^{-6}

Table 2.3: The relative RMS of the core, end and total bending fields of the maps taken at $T = 34^oC$ is shown for different nominal energies.

probes do not necessarily lock at all energies. An estimate of the integrated field can then be obtained for each reference NMR probe:

$$\int B \cdot dl_{NMR\ i} = \frac{\overline{B^i_{ref}} - c_i}{m_i}, \tag{2.20}$$

The arithmetic mean of the $\int B \cdot dl_{NMR\ i}$ from locking probes is used as an estimate $\int B \cdot dl^{\rm NMR}_{\rm Spect}$ of the bending field of the magnet. The relative residuals of these estimates to the total measured integrated field, defined as:

$$Residual\left(\int B \cdot dl_{\rm Spect}\right) = \frac{\int B \cdot dl^{\rm NMR}_{\rm Spect} - \int B \cdot dl^{\rm Meas}_{\rm Spect}}{\int B \cdot dl^{\rm Meas}_{\rm Spect}}, \tag{2.21}$$

give an RMS of $\sim 2.8 \times 10^{-5}$ for the sample of all the maps. However, if the maps are split into two samples according to their running temperature it can be seen that each sample has residuals with an RMS of $\sim 1.7 \times 10^{-5}$ with mean values offset by $\sim 4.8 \times 10^{-5}$, as is shown in Figure 2.14. This effect is attributed to the difference in temperature coefficients between the core of the magnet and the end field, which gives temperature dependent field changes which are not traced by the reference NMR probes.

Temperature effects

The temperature of the magnet clearly has an effect on the relation between the measured integrated field and that inferred from the stationary probes. It is neces-

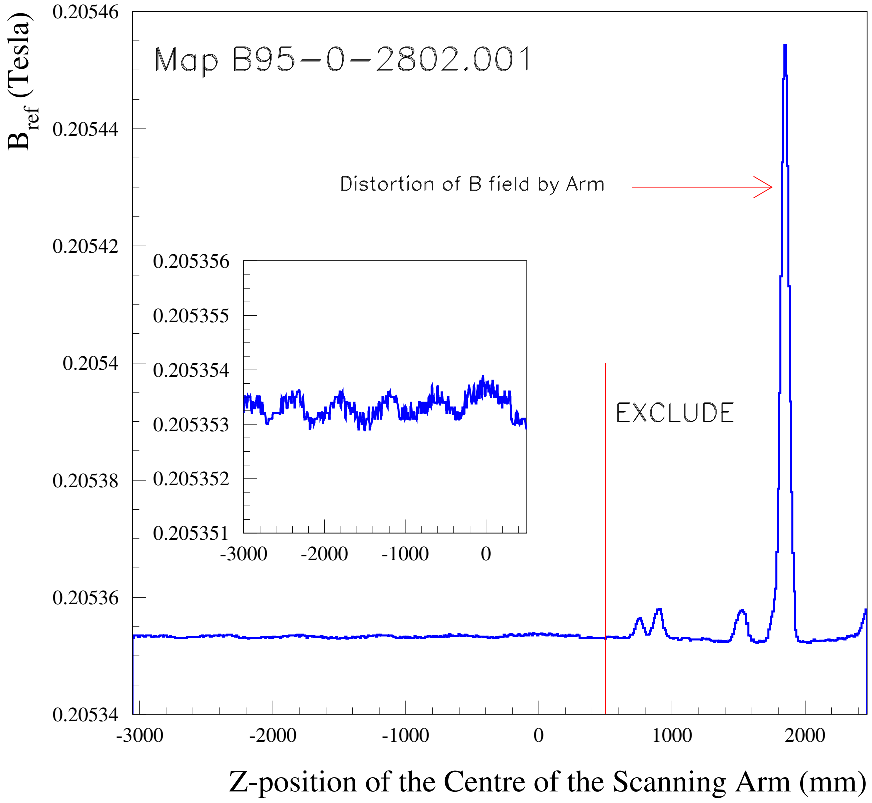

Figure 2.13: Value of the field, B^i_{ref}, in a stationary NMR probe as a function of the position of the moving scanning arm. The effect of the scanning arm as it passes over the stationary NMR probe can be seen as a series of bumps, each one corresponding to a magnetic element of the arm. The largest peak is due to the passage of the traveling NMR over the stationary one providing the field values. NMR readings from this region are excluded from the calculation of the mean. The inset shows the region which is included in the mean.

sary to account for this effect in the $\int B \cdot dl_{\mathrm{Spect}}$ model. The procedure adopted to include temperature effects is outlined below.

Most standard maps were taken such that the temperature of the coil (T_{coil}) of the magnet was 34.0^{o}C to $\pm$0.2^{o}C (RMS). In order to gauge temperature dependent effects in the magnet, a series of maps with higher operating temperatures was also taken, this time with $T_{coil} \approx 42^o$C, but with a larger spread of $\pm 0.8^o$C (RMS). The reference NMR probes trace the field changes in the core of the magnet and so their readings vary with temperature T according to:

$$B^i_{ref}(T) \;=\; (1 + C_T^{core}\Delta T)B^i_{ref}(T_0) \;=\; \beta B^i_{ref}(T_0), \qquad (2.22)$$

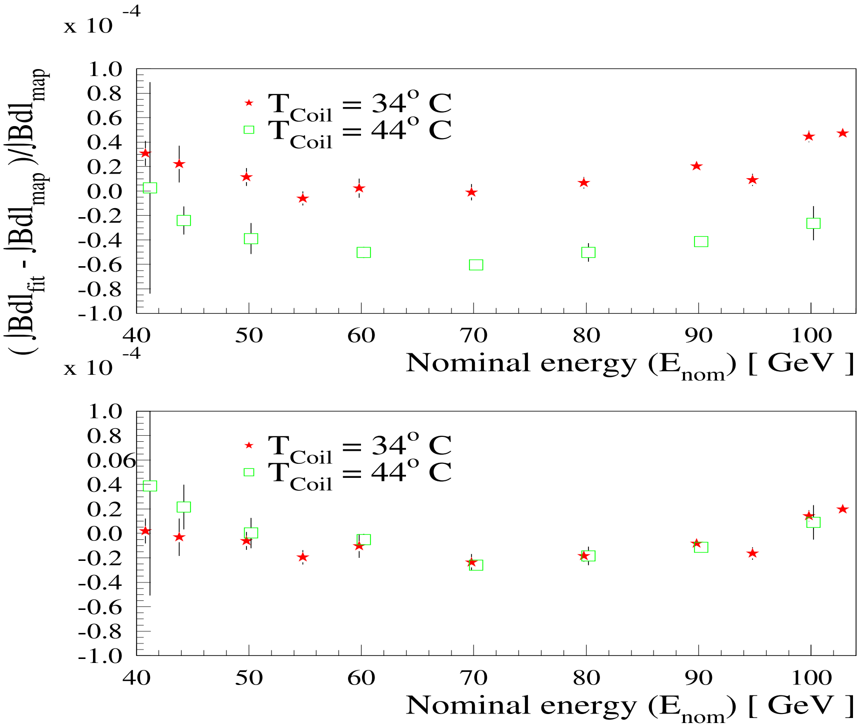

Figure 2.14: Relative residuals from Reference probe fits to measured integrated bending fields. Maps are separated according to temperature. The top plot shows the residuals from a fit where no temperature effects are taken into account. The bottom plot shows the residuals when fit coefficients and reference probe readings have been scaled according to Equation 2.32.

where C_T^{core} is the temperature coefficient of the core region, defined as $C_T^{core} = \Delta B/(B_0 \Delta T)$, ΔT is $(T - T_0)$, T_0 is $34^o C$, the mean coil temperature at which the standard maps were taken, B_0 is the B field measured at T_0 and $\beta = (1 + C_T^{core}\Delta T)$ is defined for simplicity. However, the change in total integrated field $\int B \cdot dl_{\text{Spect}}$ has both core and end-field components and so its variation with temperature is more complex:

$$\int B \cdot dl_{\text{Spect}}(T) = \{1 + \Delta T(f_{core} C_T^{core} + f_{end} C_T^{end})\} \int B \cdot dl_{\text{Spect}}(T_0) \quad (2.23)$$

$$= \{1 + \Delta T(C_T^{core} + f_{end}(C_T^{end} - C_T^{core}))\} \int B \cdot dl_{\text{Spect}}(T_0) \quad (2.24)$$

$$= \{\beta + \gamma\} \int B \cdot dl_{\text{Spect}}(T_0),$$

where f_{core} and f_{end} are the fraction of $\int B \cdot dl_{\text{Spect}}$ due to the core and end-fields respectively, *measured at* T_0, $\gamma = f_{end}(C_T^{end} - C_T^{core})\Delta T$, and the relation $f_{end} + f_{core} = 1$ has been used. The coil temperature T is the same for core and end-field[7].

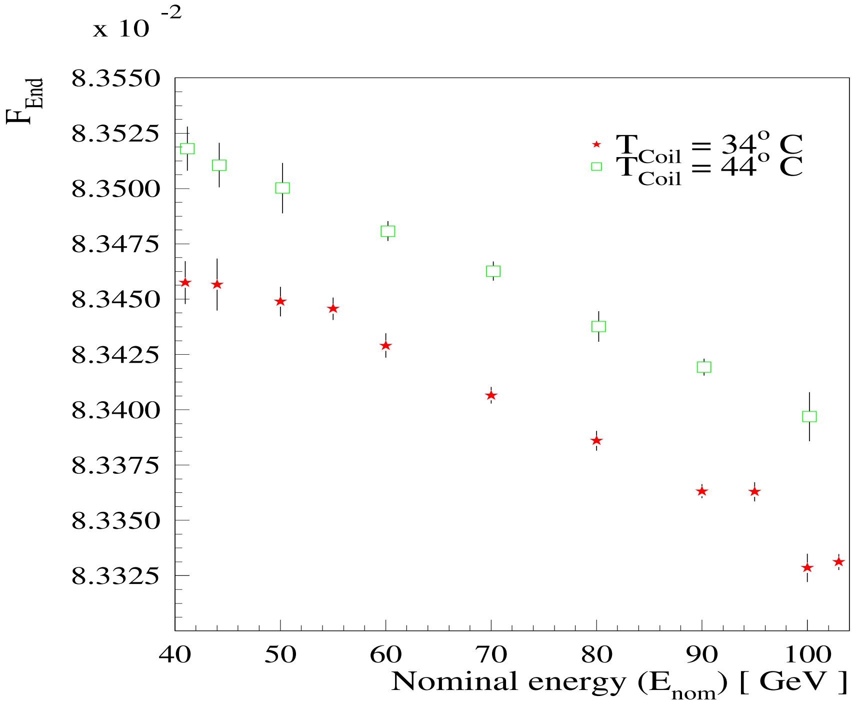

Figure 2.15: Fraction of the total bending field of the spectrometer dipole magnet due to the end-field contribution for the two temperature regimes.

In order to take these effects into account the relation 2.19 must be modified. This is achieved by transforming the B^i_{ref} values to an arbitrary reference temperature, T_0, before performing the linear fit in Equation 2.19. Requiring that the integrated field inferred from the reference probes through Equation 2.20 follows the temperature dependence given in Equation 2.25 yields:

$$\frac{\beta B^{i\ corr}_{ref} - c_i}{m_i} = \{\beta + \gamma\} \int B \cdot dl_{\text{Spect}}(T_0) = \{\beta + \gamma\} \frac{B^i_{ref} - c_i}{m_i}, \tag{2.25}$$

where $B^{i\ corr}_{ref}$ are the transformed reference probe readings. A linear scaling factor α is sought such that $B^{i\ corr}_{ref} = \alpha B^i_{ref}$. Using Equation 2.25, α can be expressed as:

$$\alpha = \frac{(\beta + \gamma)(B^i_{ref}(T) - c_i) - c_i}{\beta B^i_{ref}(T)} \tag{2.26}$$

$$\approx 1 + \frac{\gamma}{\beta} \tag{2.27}$$

[7]A global temperature is used here so all temperature effects are absorbed into the temperature coefficients.

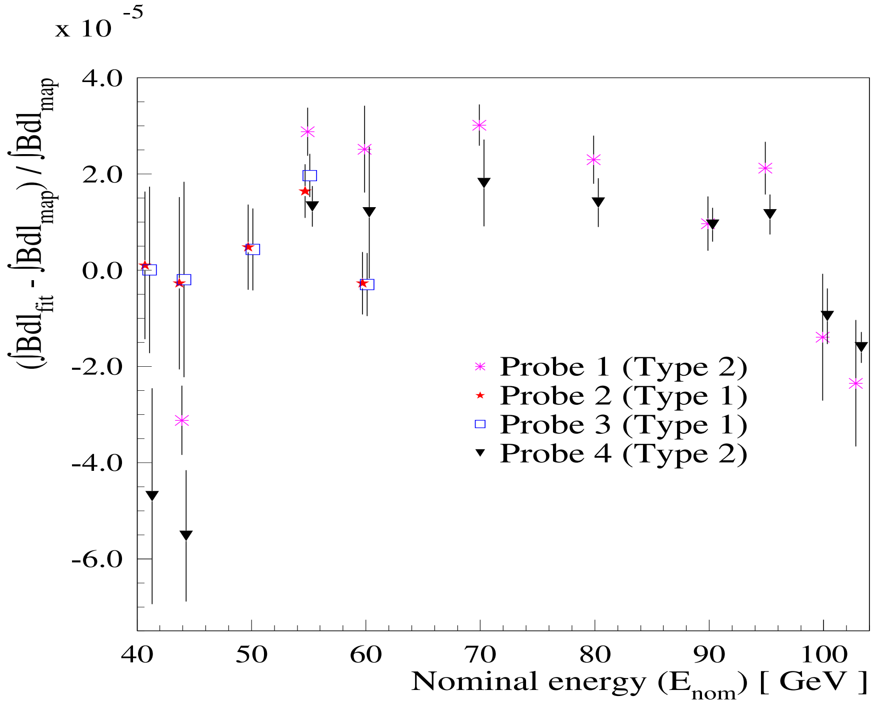

Figure 2.16: Relative residuals from the linear fit of each of the reference NMR probe readings to the measured integrated field. These residuals are used to provide probe-by-probe offset corrections before the probe estimates of $\int B \cdot dl$ are combined to get $\int B \cdot dl_{\mathrm{Spect}}$.

$$= \quad 1 + \frac{f_{end}(C_T^{end} - C_T^{core})\Delta T}{1 + C_T^{core}\Delta T} \tag{2.28}$$

$$\approx \quad 1 + f_{end}(C_T^{end} - C_T^{core})\Delta T \tag{2.29}$$

where the approximations $c_i \approx 0$ and $1 + C_T^{core}\Delta T \approx 1$ have been made in going from 2.26 to 2.27 and 2.28 to 2.29 respectively. An effective temperature coefficient C_T^{eff} is then calculated by inspection of Equation 2.29:

$$C_T^{eff} = f_{end}(C_T^{end} - C_T^{core}), \tag{2.30}$$

Temperature coefficients C_T^{core} and C_T^{end} were estimated at each nominal energy point for which maps were taken at both nominal temperature values by performing a linear fit according to:

$$\int B \cdot dl = (C_T T + 1) \int B \cdot dl(T_0). \tag{2.31}$$

The fitted values are used to estimate the mean value of $(C_T^{end} - C_T^{core})$. This quantity, together with the mean values of C_T^{core} and C_T^{end}, is shown in Table 2.5. The

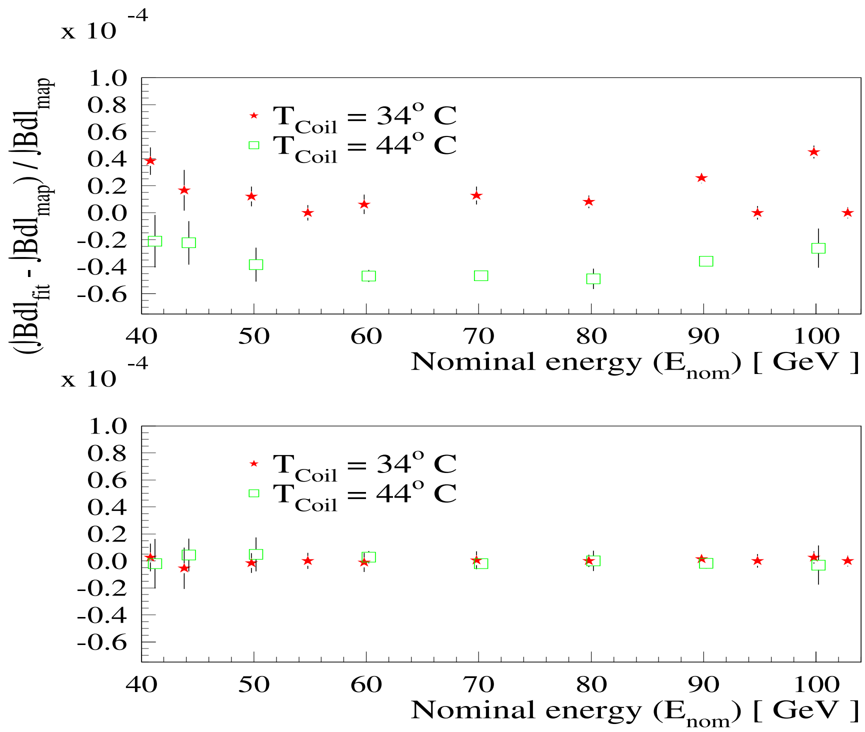

Figure 2.17: Relative residuals from Reference probe fits to measured integrated bending fields after correcting for probe-by-probe offset in bins of energy. As with Figure 2.14, the top plot shows the residuals from a fit where no temperature effects are taken into account, and the bottom plot shows the residuals when fit coefficients and reference probe readings have been scaled according to Equation 2.32.

reference NMR readings are then re-scaled according to:

$$B^{i\ corr}_{ref} = (1 + C^{eff}_T (T - T_0)) B^i_{ref}, \tag{2.32}$$

before performing the linear fit defined by Equation 2.19. However, the calculation of C^{eff}_T has to account for the dependence of the fractional end field f_{end} on the magnet excitation current. The evolution of f_{end} with nominal energy for the two different temperature samples can be seen in Figure 2.15. It is clear that the f_{end} term in Equation 2.30 has a slope that has to be taken into account. The procedure followed is to perform a linear fit to relate f_{end} to the nominal energy, E_{nom}:

$$f_{end} = M_{end}(E_{nom} - 41\text{GeV}) + C_{end}. \tag{2.33}$$

The resulting coefficients are used to estimate the value of f_{end} given the nominal energy during a spectrometer measurement. They are summarised in Table 2.6. In

Probe (Type)	m (Tm^{-1})	c (T)	$\rho_{m,c}$
NMR_1 (2)	$17075532 \pm 7 \times 10^{-8}$	$-4312 \pm 8 \times 10^{-8}$	-0.991
NMR_2 (1)	$17068200 \pm 52 \times 10^{-8}$	$-1383 \pm 32 \times 10^{-8}$	-0.992
NMR_3 (1)	$17067944 \pm 26 \times 10^{-8}$	$-1659 \pm 16 \times 10^{-8}$	-0.991
NMR_4 (2)	$17079301 \pm 10 \times 10^{-8}$	$-3100 \pm 10 \times 10^{-8}$	-0.980

Table 2.4: The calibration parameters and correlation coefficients of the two parameter fit of mean NMR_{ref} values to the measured total bending fields. The fit is performed individually for each of the reference probes including every available energy point. For the Type 1 probes this means energies up to 60 GeV. The Type 2 probes were operational at all energies for the mapping campaign but radiation damage in the LEP tunnel increases their locking threshold.

Mean Temperature Coefficient	Value (K^{-1})
$\overline{C_T^{core}}$	$-8.62 \pm 4.52 \times 10^{-6}$
$\overline{C_T^{end}}$	$7.81 \pm 0.82 \times 10^{-5}$
$\overline{C_T^{end} - C_T^{core}}$	$8.67 \pm 0.56 \times 10^{-5}$

Table 2.5: Mean Temperature coefficients for the end and core fields of the LEP spectrometer magnet. Note the opposite signs of the end and core coefficients. The mean of the difference between core and end-field coefficients is is used to correct the $\int B \cdot dl$ of the magnet for temperature variations about 34^oC.

practice, the magnet current is used to get a value for the nominal energy using a linear factor. Then C_T^{eff} can be calculated using Equation 2.30.

The final coefficients m_i and c_i are shown in Table 2.4, together with their associated errors and correlations. In order to extract $\int B \cdot dl^{\mathrm{NMR}}_{\mathrm{Spect}}$ values from a given set of B_{ref} readings the scaling described in Equation 2.32 is applied before using the coefficients m and c. All three temperature coefficients are shown in Table 2.5. Note the opposite sign of the end and core field coefficients. The relative residuals with and without the temperature correction are shown in Figure 2.14.

Offset Corrections

After applying the temperature correction, the RMS of the relative residuals for the full sample is reduced from $\sim 2.8 \times 10^{-5}$ to $\sim 1.7 \times 10^{-5}$. The offset in the mean values is reduced from $\sim 4.8 \times 10^{-5}$ to $\sim 1.1 \times 10^{-5}$. It is clear that, with or without the temperature correction, the residuals reflect a nonlinearity in the relation between reference probe values and measured integrated bending field. The structure of the residuals for each one of the probes can be seen in Figure 2.16. For this reason, correction factors are calculated for the estimated field from each

T_{coil}	$M_{end}(\mathrm{GeV}^{-1})$	C_{end}	$\rho_{M,C}$
34	$-2.21 \pm 0.02 \times 10^{-6}$	$83470.35 \pm 1.06 \times 10^{-6}$	-0.926
44	$-2.07 \pm 0.03 \times 10^{-6}$	$83519.36 \pm 1.51 \times 10^{-6}$	-0.933

Table 2.6: The parameters and correlation coefficients of the linear fit of the fractional end-field of the spectrometer magnet, f_{end}, against the nominal energy. The coefficients correspond to Equation 2.33. Only the coefficients for the 34^oC maps are used for the analysis. The 44^oC coefficients are included to show that the slope is, to a good approximation, independent of temperature.

probe in bins of energy and applied to the estimation of the mean $\int B \cdot dl^{\mathrm{NMR}}_{\mathrm{Spect}}$. These corrections further reduce the RMS of the relative residuals to $\sim 1.1 \times 10^{-5}$, remove the overall bias, and do away with the need to reject outliers[8]. The residuals with the offset correction applied, with and without the temperature corrections, are shown in Figure 2.17.

In order to test the validity of the linear fit coefficients calculation and of the residual offsets correction, the fit defined by Equation 2.19 and the calculation of the residuals was carried out using half the available maps, and the remaining maps were fitted with all corrections applied. The resulting mean relative residual was found to be $(0.52 \pm 3.52(RMS)) \times 10^{-5}$ without offset corrections and $(0.30 \pm 1.23(RMS)) \times 10^{-5}$ with offset corrections, for all energies and operating temperatures. The residuals for both the full standard map sample and the independent subsample containing half the maps, after applying the offset corrections, can be seen in Figure 2.18. The reduction in the mean and RMS of the independent sample after applying the offset corrections gives an indication of the reproducibility of the structure of the residual distribution seen in figure 2.16 and underlines the validity of using such corrections.

Transverse position of the beam

In addition to temperature effects, any variation of the bending field strength in the transverse (x) and vertical (y) directions of the dipole magnet would give rise to changes in the relation between the NMR probe readings and the integrated bending field of the magnet. Since the beam necessarily describes a 3.8mrad arc inside the

[8] The outliers are caused by the large residuals shown by the Type 2 probes at energies under 50 GeV.

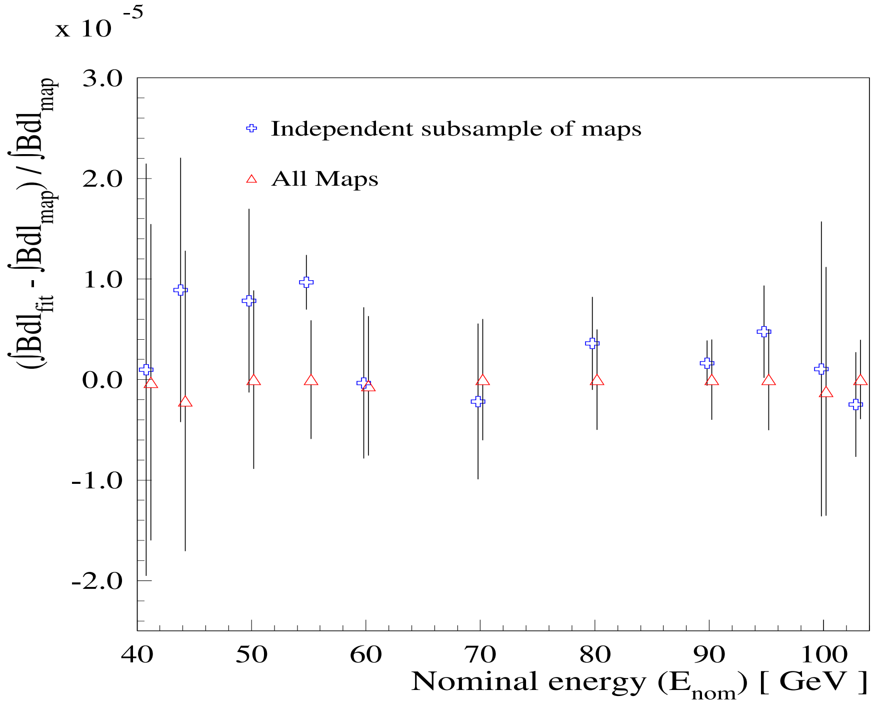

Figure 2.18: Relative residuals from Reference probe fits to measured integrated bending fields after correcting for probe-by-probe offset in bins of energy. Two sets of residuals are shown. The first corresponds to a subsample of $\sim$ 150 maps where the offset corrections and calibration coefficients from Equation 2.19 have been obtained from an independent sample of maps. The second set corresponds to the full sample of maps where the same sample has been used to calculate coefficients and offset corrections.

total dipole bending field, it probes regions displaced in x relative to the nominal axis along which the standard maps were taken. For a total bending field length of $\sim$6.2m the x displacement of the beam is $\sim$6mm. In order to take this effect into account, a series of maps were made with the measuring arm displaced in x. They covered a range of 20mm and were taken at three different excitation currents, corresponding to 45, 60 and 100 GeV. Whereas relative differences in end and core integrated fields of $\sim 10^{-5}$ were observed, the sign of the shifts is different between end and core fields and so largely cancels out. The relative shifts to the total bending field lie between 0.5×10^{-6} and 1.0×10^{-6}. Given the size of this effect, it was deemed unnecessary to include any modelling of the x dependence of the field into the $\int B \cdot dl_{\mathrm{Spect}}$ calculation.

The $\int B \cdot dl_{\text{Spect}}$ model

Using the calibration coefficients calculated from Equation 2.19, mean values of the readings from each of the four reference NMR probes, the mean temperature of the coil of the magnet and the DC excitation current[9], $\int B \cdot dl^{\text{NMR}}_{\text{Spect}}$ can then be calculated as follows:

- Re-scale each of the mean NMR$_{ref}$ values using the temperature correction described in Equation 2.32.
- Use the calibration coefficients from Table 2.4 and Equation 2.20 to estimate a total bending field $\int B \cdot dl_{NMR\ i}$ for each available reference NMR probe.
- Use the DC excitation current to calculate the nominal energy of the spectrometer magnet.
- Apply offset corrections to reduce the residuals seen in Figure 2.16 to each of the available $\int B \cdot dl_{NMR\ i}$ according to the nominal energy of the magnet.
- Take an arithmetic mean of the offset-corrected $\int B \cdot dl_{NMR\ i}$ to get $\int B \cdot dl^{\text{NMR}}_{\text{Spect}}$.

The relative accuracy on the prediction of the bending field of the spectrometer magnet from the $\int B \cdot dl_{\text{Spect}}$ model can now be determined from the residuals of the independent samples of standard maps. It is found to be $1.2 \times 10^{-5} (RMS)$. However, the quantity of interest in performing a beam energy measurement with the spectrometer is the ratio of two integrated bending fields, one at resonant depolarisation and the other at physics energy. Therefore the error on E_{BEAM} due to the estimation of the bending field of the dipole is calculated from:

$$\frac{\int B \cdot dl_{meas}|_{E_{Phys}}}{\int B \cdot dl_{meas}|_{E_{RDP}}} - \frac{\int B \cdot dl_{Spect}|_{E_{Phys}}}{\int B \cdot dl_{Spect}|_{E_{RDP}}}, \tag{2.34}$$

where $\int B \cdot dl_{meas}$ is the integrated bending field of the spectrometer dipole as measured by the traveling arm. To estimate the mean and RMS of the quantity in expression 2.34, an independent sample of maps was separated according to nominal energy

[9]The DC excitation current is used in order to determine the nominal energy the spectrometer is operating under in order to apply the offset corrections given by the fit residuals seen in Figure 2.16.

Nominal E_{BEAM}	41	44	50	55	60
70	0.53 ±3.57	1.76 ±2.34	1.40 ±1.59	1.51 ±0.98	0.22 ±1.19
80	-0.50 ±3.92	0.83 ±2.28	0.68 ±1.57	0.88 ±0.72	-0.52 ±1.13
90	-0.14 ±4.33	1.49 ±2.66	1.12 ±1.62	1.31 ±0.48	-0.30 ±1.13
95	-0.87 ±4.66	-0.89 ±2.92	0.58 ±1.85	0.84 ±0.83	-0.81 ±1.32
100	1.44 ±4.25	1.64 ±3.69	0.74 ±3.22	1.57 ±2.68	-0.16 ±2.64
103	0.85 ±5.07	2.66 ±3.16	2.12 ±1.99	2.27 ±0.90	0.37 ±1.42

Table 2.7: The mean values of expression 2.34 are given in units of 10^{-5}. All errors are derived from the RMS spread of the results for all available combinations of maps, and give an indication of the accuracy to which the ratio between integrated bending fields can be predicted. The overall estimate of the accuracy for all combinations of maps is $\sim 3 \times 10^{-5}$.

into an E_{RDP} and an $E_{Physics}$ groups[10]. The quantity in expression 2.34 was evaluated for all possible cross-group combinations of maps. The mean and RMS were then calculated for all possible energy combinations. The results are summarised in Table 2.7. The overall evaluation of expression 2.34 is $(0.30 \pm 3.00) \times 10^{-5}$. The above procedure is a conservative indicator of the overall accuracy to which the NMR calculations can resolve ratios of bending fields, since it includes fill to fill variations in the bending field. Since the spectrometer is calibrated on a fill by fill basis during beam energy calibration, these variations are not present in the real calibration data. A similar study was performed with sets of maps taken during single magnet ramp cycles. However, the statistics of the study are small and no significant difference in the resolution could be observed.

Measurement of $\int B \cdot dl_{\text{Spect}}$ with a Traveling Mole

In order to test the compatibility between the magnetic measurements carried out on the LEP spectrometer magnet at the ISR tunnel with the behaviour of the magnet

[10]The separation was done such that maps with nominal energies less than or equal to 60 GeV were included in the E_{RDP} group. All remaining maps were included in the E_{Phys} group.

inside the LEP tunnel, and as a cross check to the analysis described above, a separate campaign to map the total bending field of the magnet was carried out, this time with a chariot carrying NMR probes and moving along a mock beam pipe section. Such a device is known as a "magnet mole" or "traveling mole". The details of this analysis can be found in [40]. Equipped with one Type 1 and one Type 2 NMR probe for measuring the core bending field, and with a search coil for measuring the fringe fields, the traveling mole was used to measure the integrated bending field of the spectrometer magnet both in the ISR tunnel and in LEP under different operating conditions. Linear fits like those defined by Equation 2.19 were performed and the residuals checked. It was found that the two mapping set-ups are compatible giving similar residual distributions. From fits to all available maps from both methods a relative error on the predicted bending field of 3×10^{-5} is obtained from the RMS of expression 2.34, in agreement with the resolution found using the measuring arm measurements. This is the only test of the reproducibility of field predictions after the magnet was moved to the LEP tunnel and it is chosen as the final estimate of the relative accuracy to which $\int B \cdot dl_{\mathrm{Spect}}$ can be predicted.

2.7.6 Analysis of 1999 Data

Five multi-point fills, including at least one RDP measurement and one high energy point, were taken in 1999. From these, the performance of the spectrometer in the RDP region was estimated. The spectrometer was found to be unbiased in this regime, with an uncertainty, given by the RMS spread of the results, of 8 MeV:

$$E_{Spect} - E_{RDP} = 3.0 \pm 8.0 \text{ MeV}(RMS), \tag{2.35}$$

The quantity $E_{Spect} - E_{RDP}$ is shown for the five fills in Figure 2.19. Two of these five multi-point fills were ramped to physics energies and spectrometer measurements carried out. Together with one two-point fill with one measurements at RDP energy and one at high energy, these fills were used to measure the deviation of E_{BEAM} as predicted by the spectrometer from the value predicted by the NMR extrapolation method. The results for each of the three fills can be seen in Figure 2.20. The

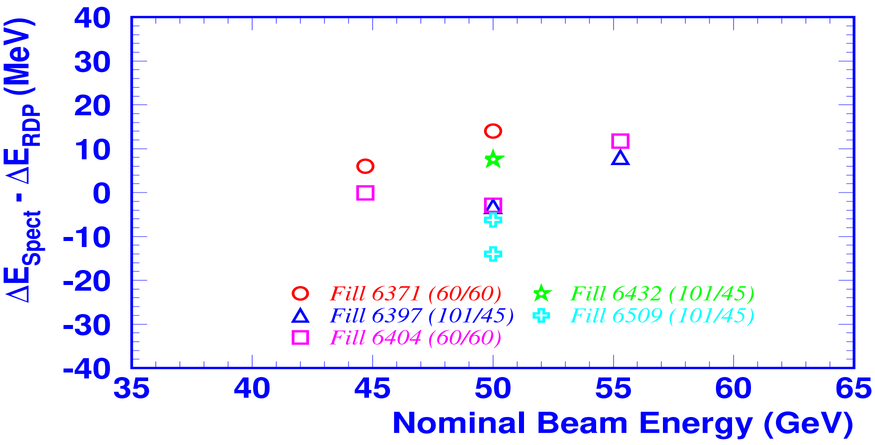

Figure 2.19: Difference between energy *intervals* measured by RDP and the LEP Spectrometer for different calibration energies. The first RDP point (41 GeV) is omitted as it is used to calibrate the spectrometer and so has zero difference by definition.

spectrometer is found to be unbiased with respect to the NMR method, this time with an RMS uncertainty of 15 MeV:

$$E_{Spect} - E_{NMR} = 0.5 \pm 15.0 \text{ MeV}(RMS), \tag{2.36}$$

It must be pointed out that these numbers are based on the limited statistics of the 1999 data sample. Therefore the uncertainty on the RMS spread of the results given in 2.35 and 2.36 is large. Furthermore, the Spectrometer is under development and the data analysis and calibrations are by no means final at the time of writing. Therefore all numbers concerning uncertainties are preliminary. No attempt has been made to assign an uncertainty from the BPM bend angle analysis or the RF corrections. Both are expected to be larger than the uncertainty due to the measurement and modelling of the integrated bending field presented in this analysis.

2.7.7 Conclusions

The integrated bending field of the spectrometer has been mapped. A model of the bending field during LEP operations has been developed and shown to give predictions of $\int B \cdot dl_{\text{Spect}}$ well within the tolerance required for the beam energy

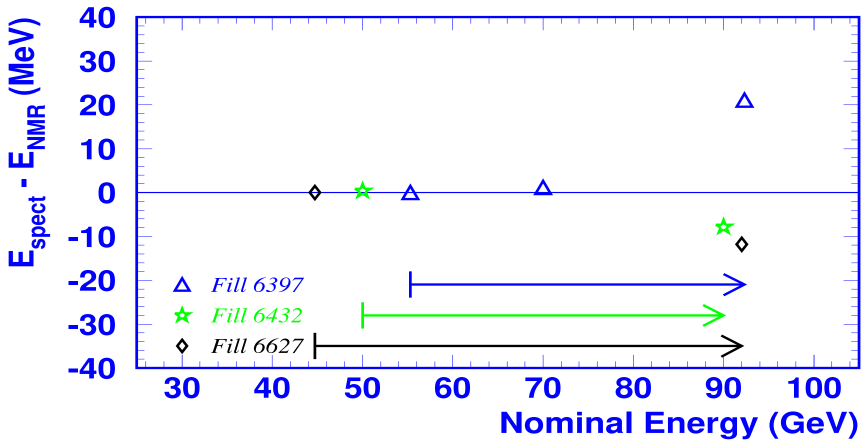

Figure 2.20: Difference between beam energy estimates from the LEP Spectrometer and the NMR method in fills with RDP and high energy points.

determination. The uncertainties due to the measurement of the bend angle of the beam and the RF model corrections used in the E_{BEAM} measurement strategy are under investigation. There are clear indications that these are larger than the uncertainty on $\int B \cdot dl_{\mathrm{Spect}}$ and therefore the dominant sources of error. The data of 1999 has been analysed to test performance of the spectrometer. The 15.0 MeV error on $E_{Spect} - E_{NMR}$ given in Equation 2.36 gives a preliminary confirmation of the feasibility of the Spectrometer as a means to test the validity of the linearity assumption which forms the basis of the NMR extrapolation method. Although the statistics are limited and there is scope for improvement in precision, these first Spectrometer results seem to confirm the NMR extrapolation method.

2.8 The Synchrotron Tune Q_s

The Synchrotron tune Q_s is defined as the ratio of the synchrotron oscillation angular frequency of a bunch in a storage ring, Ω, and the revolution angular frequency, ω_{LEP} $(= 2\pi f_{LEP})$. It is an observable that is dependent on the energy loss per turn, U_0, which is itself directly dependent on the beam energy:

$$U_0 = \left(\frac{C_\gamma}{\rho}\right) \; E^4_{Beam}, \tag{2.37}$$

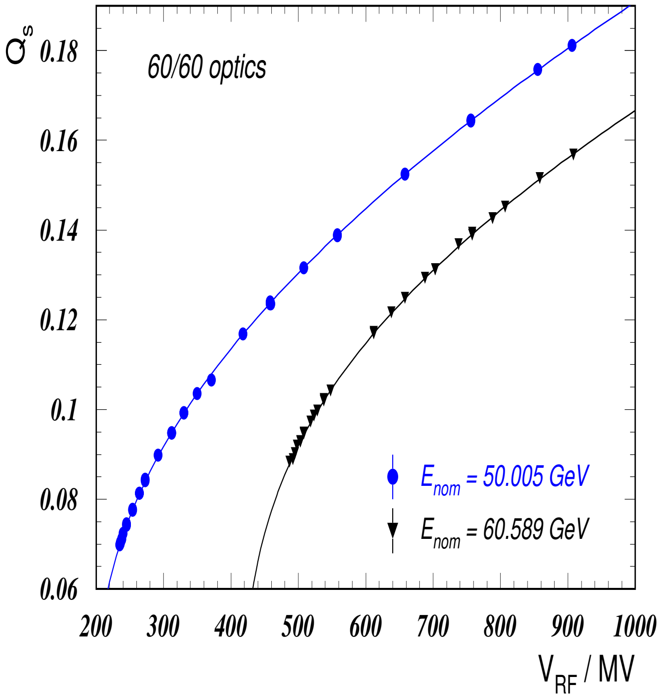

Figure 2.21: Measurements of Q_s as a function of the total effective accelerating voltage V_{RF}. Data points for two energies are superimposed on curves representing the fitted function described by Equation 2.38.

where C_γ is constant for each particle type and ρ is the mean bending radius of the charged particles. The synchrotron tune Q_s can be expressed as [41]:

$$Q_s^2 \;=\; \left(\frac{\alpha_c h}{2\pi E_{Beam}}\right)\sqrt{e^2V_{RF}^2 \;+\; bV_{RF}^4 \;-\; (U_0+K)^2}, \tag{2.38}$$

where α_c is the momentum compaction factor, h is the harmonic number[11], V_{RF} is the total RF voltage, and K takes into account energy losses due to sources different to synchrotron radiation in the LEP dipole magnets, like synchrotron radiation due to the dipole component of quadrupole and corrector magnets and the resistive part of the longitudinal impedance arising from beam-induced parasitic modes. The V_{RF}^4 term accounts for the inhomogeneous distribution of the RF voltage around LEP. Q_s is measured from a Fourier analysis of the measured phase difference between a bunch and the RF frequency. The Fourier analysis is performed with a spectrum

[11]The harmonic number h, relating the revolution frequency f_{LEP} and the RF frequency f_{RF} through $f_{RF} = hf_{LEP}$, is 31320 for the LEP ring.

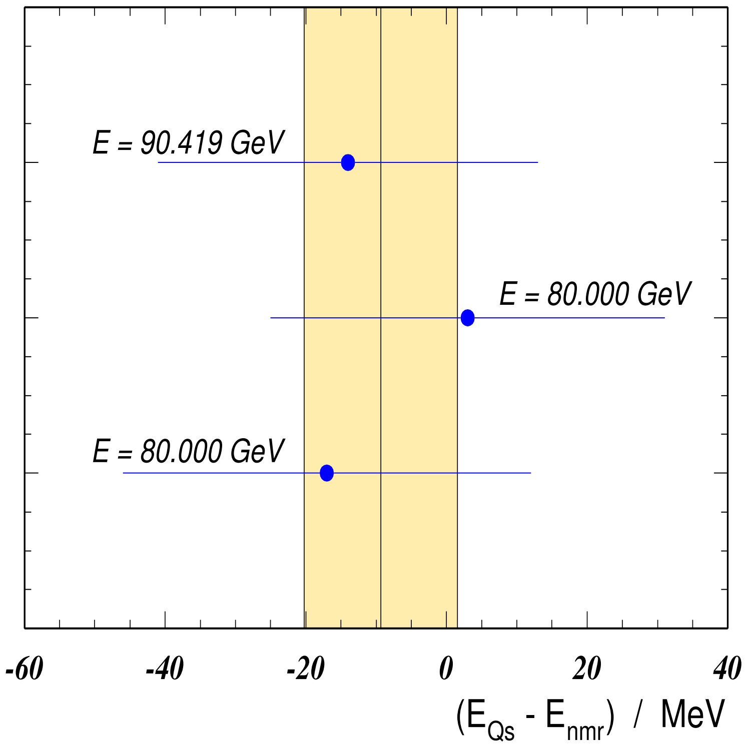

Figure 2.22: Differences between Q_s and NMR model measurements of E_{BEAM} for the three Q_s measurements performed in 1998 and 1999. The vertical line and band give the average value and statistical scatter of the measurements.

analyser, and the Q_s peak extracted manually, as spurious spikes in the signal make a fully automated measurement impossible. In practice the measurement is averaged over many turns and all bunches. The uncertainty on the measurement of Q_s is dominated by the manual reading, which has an RMS scatter of 3×10^{-4}. Q_s is fitted against V_{RF} according to Equation 2.38 in order to extract E_{BEAM}. Low energy voltage scans are made to calibrate V_{RF} against the NMR model. The measurement is then carried out with a voltage scan at high energy. The correction factors present in Equation 2.38 are obtained from dedicated measurements and from model simulations. A measurement with V_{RF} scans at two different energies can be seen in Figure 2.21. The sensitivity of this method is $\sim$ 25 MeV and, to a good approximation, independent of energy. The sources of error are the statistical component which comes in as the error in the fit of expression 2.38, uncertainties in the modelling of the total additional energy loss K, the calibration of V_{RF} against the NMR model, and the determination of machine parameters α_c and ρ. There is scope for reducing the error by better understanding the systematic uncertainties.

This method was used to determine E_{BEAM} at high energy in 1998, 1999 and 2000. The results from the first two years can be seen in Figure 2.22. It can be seen that the agreement between the two methods is very good The combined difference between the values of E_{BEAM} predicted by the Q_s method and the NMR model is:

$$E_{Q_S} \ - \ E_{NMR} \ = \ -9 \ \pm \ 11 \text{ MeV } (RMS). \tag{2.39}$$

With three measurements, the uncertainty on the RMS scatter of the measurements is quite large. However, the results seem compatible with the NMR model and very encouraging. At the time of writing further analysis involving the measurements taken in 2000 is underway with a view towards improving both the statistical and systematic sensitivity of the method.